Citation
Tian, W. and Zhang, H. and Sun, H. and Suvorova, A. and Saunders, M. and Tade, M. and Wang, S. 2016. Heteroatom (N or N-S)-Doping Induced Layered and Honeycomb Microstructures of Porous Carbons for CO2 Capture and Energy Applications. Advanced Functional Materials. 26 (47): pp. 8651–8661 . http://doi.org/10.1002/adfm.201603937

Heteroatom (N or N-S)-Doping Induced Layered and Honeycomb Microstructures of Porous Carbons for CO_2 Capture and Energy Applications

Wenjie Tian, Huayang Zhang, Hongqi Sun, Alexandra Suvorova, Martin Saunders, Moses Tade, and Shaobin Wang**

W. Tian, H. Zhang, Prof. M. Tade, Prof. S. Wang

Department of Chemical Engineering and CRC for Contamination Assessment and Remediation of the Environment (CRC CARE), Curtin University, GPO Box U1987, WA 6845, Australia
E-mail: shaobin.wang@curtin.edu.au

Assoc. Prof. H. Sun

School of Engineering, Edith Cowan University, 270 Joondalup Drive, Joondalup, WA 6027, Australia

E-mail: h.sun@ecu.edu.au

Dr. A. Suvorova, Assoc. Prof. M. Saunders

Centre for Microscopy, Characterization and Analysis, The University of Western Australia, Crawley, WA 6009, Australia

Keywords: *Heteroatom-doping, Pillared-layer carbon, Honeycomb carbon, CO_2 capture, ORR*

ABSTRACT

Increasing global challenges such as climate change, environmental pollution and energy shortage have stimulated the worldwide explorations into novel and clean materials for their applications in the capture of carbon dioxide, a major greenhouse gas, and toxic pollutants, energy conversion and storage. In this study, two microstructured carbons, namely N-doped pillaring layered carbon (NC) and N, S co-doped honeycomb carbon (NSC), have been fabricated through a one-pot pyrolysis process of a mixture containing glucose, sodium bicarbonate, and urea or thiourea. The heteroatom doping was found to induce tailored microstructures featuring highly interconnected pore frameworks, high sp^2-C ratios, and high surface areas. The formation mechanism of the varying pore frameworks is believed to be hydrogen-bond interactions. NSC displays a similar CO_2 adsorption capacity (4.7 mmol g^{-1} at 0 °C), a better CO_2/N_2 selectivity and higher activity in oxygen reduction reaction (ORR) as compared with NC-3 (the NC sample with the highest N content of 7.3%). NSC favors an efficient four-electron reduction pathway and presents better methanol tolerance than Pt/C in alkaline media. The porous carbons also exhibit excellent rate performance as supercapacitors.

1. Introduction

Efficient CO_2 capture and sequestration become more and more critical for climate change mitigation, atmospheric pollution control in enclosed spaces, mining safety, and production processes of synthetic fuels and high valued chemicals.[1-3] Conventional CO_2 removal employs amine-based solvents to absorb CO_2 from exhaust gas,[4] yet the technique suffers from inherent drawbacks, for examples, intensive energy input, low thermal stability of solvents, equipment

corrosion and inefficiency, volatility of the amines and toxicity.[4, 5] Thus, novel materials with a high CO_2 uptake capacity but featuring a lower energy penalty for regeneration would be crucial for improving commercial viability. Recently, the development of porous solid adsorbents has attracted considerable attention. A variety of solid materials such as metal organic frameworks (MOFs),[6] zeolites,[7] porous carbons,[2, 8] and coordination organic polymers (COPs)[9] have been developed for CO_2 uptake. Among them, porous carbons have been demonstrated to be of low cost and have excellent thermal and chemical stability, a hydrophobic surface, high surface area, absence of toxicity and cost-effective regeneration for CO_2 uptake.

On the other hand, in order to mitigate CO_2 emissions from fossil fuel combustion, the deployment of renewable and clean energy sources such as H_2 can be a promising alternative. Therefore, suitable energy conversion and storage technologies are highly in demand. Among these approaches, fuel cells have been recognized to possess the cleanest and most efficient energy conversion. In the processes the fuels react with O_2 through benign electrochemical processes at a high fuel-conversion efficiency, avoiding direct combustion.[10, 11] Oxygen reduction reaction (ORR) is the cornerstone of cathode reactions in fuel cells in which an oxygen molecule receives electrons to form products.[11-13] Pt and Pt-based alloys are the most efficient ORR catalysts to date, yet the scarcity, high price, poor stability and poor tolerance of Pt catalysts to methanol severely hinder their wide-spread implementation.[13] Rational design of highly efficient non-precious catalysts with a comparable ORR activity to Pt-based alloys but a superior stability and alcohol-tolerance is a hot topic of research in this field. In this regard, carbon materials become fantastic candidates, considering their high electronic conductivity, tunable porosity, excellent stability and unique electrocatalytic selectivity.

Therefore, tremendous efforts have been devoted to developing porous carbons to address various issues such as structure-dependent mass-diffusion limitations.[14]

For CO_2 uptake and ORR applications, the performance of porous carbon materials can be affected by both the intrinsic nature and the porous structure. The intrinsic activity can be improved by introducing heteroatoms.[14, 15] Typically, nitrogen doping is most attractive since it can induce some basicity for enhanced interactions with acidic gas CO_2. Recent studies also indicated that polar sulfur-containing groups could facilitate CO_2 adsorption on carbon materials,[16] yet few investigations have been performed in CO_2 capture by porous carbons with nitrogen and sulfur doping. For ORR, N incorporation can disrupt the electro-neutrality of adjacent C atoms, creating charges and spin redistribution to favor oxygen adsorption and reduction.[14] Besides, N and S co-doping has been adopted in ORR to obtain enhanced activities compared with mono-atom doping, evidenced in experiment and simulation.[17] Despite extensive studies having been carried out, the available catalyst materials are still far from satisfactory from economical, technical and environmental viewpoints.[14, 15]

Hierarchically porous carbons with both mesopores and micropores are believed to be favored for both CO_2 uptake and ORR. Specifically, mesopores enable fast gas diffusion, while micropores induce high surface area for a high CO_2 adsorption capacity.[18] With regard to ORR, micropores can expose large amounts of potential active sites whereas mesopores are conducive for mass transfer during electrochemical reactions.[19] Soft- and hard-templating approaches have been applied to fabricate

the desired porous structures.[20] In the former synthesis, soft-templates can be easily removed by heating. Interaction between surfactant molecules and guest species is crucial for the formation of porous structures.[20, 21] Since minor variation of the synthesis condition can significantly affect the co-assembly process, the hydrolysis and condensation of guest species and their assembly with the surfactants should be carefully controlled to generate the desired porosity.[22] The hard-templating route is able to fabricate a wide variety of materials. However, it has the limitations associated with the complex and time-consuming template-removing procedures.[19, 23] To date, it still remains a challenge to rationally design and prepare hierarchically porous structures by a green and feasible protocol.[18]

Here we first propose a simple urea-sodium bicarbonate-based process to prepare N-doped, pillaring-layered porous carbons (NCs), using glucose as the carbon source. Compared with soft-templating methods, this protocol is easy to handle since the self-assembly among the precursors is effortless to happen by evaporation due to the strong hydrogen-bond interactions. In comparison with the hard-templating craft, our process based on the pore-foaming of sodium bicarbonate is evidently more green and scalable, because the decomposition product (sodium carbonate) can be easily removed by water washing. Through tailoring urea addition, the N functionalities and hierarchical porosities can be designed and optimized. NSC was prepared according to our recent report,[24] by a one-pot pyrolysis of glucose, thiourea and sodium bicarbonate at 700 °C under a nitrogen flow. NSC has a honeycomb-porous morphology and exhibits excellent performance in water treatment.[24] It is further explored for CO_2 capture and ORR tests in this work. Based on hydrogen-bond interactions, the formation mechanism of the different pore frameworks is revealed,

which is of significance for designing various porous carbon materials. Non-doped porous carbon (PC) was also prepared from glucose and sodium bicarbonate. It is indicated that all the synthesized porous carbons have a high sp^2-C ratio. With a combination of high surface areas and interconnected pore networks, they show a great potential to serve as both effective CO_2 adsorbents and metal-free electrocatalysts for ORR. In addition, to elucidate the transport issues in the ORR activity, supercapacitor measurements were also conducted. This study opens a route for the large-scale production of highly-active porous carbons.

2. Results and Discussion

2.1. Properties of Porous Carbons and Their CO_2 Capture

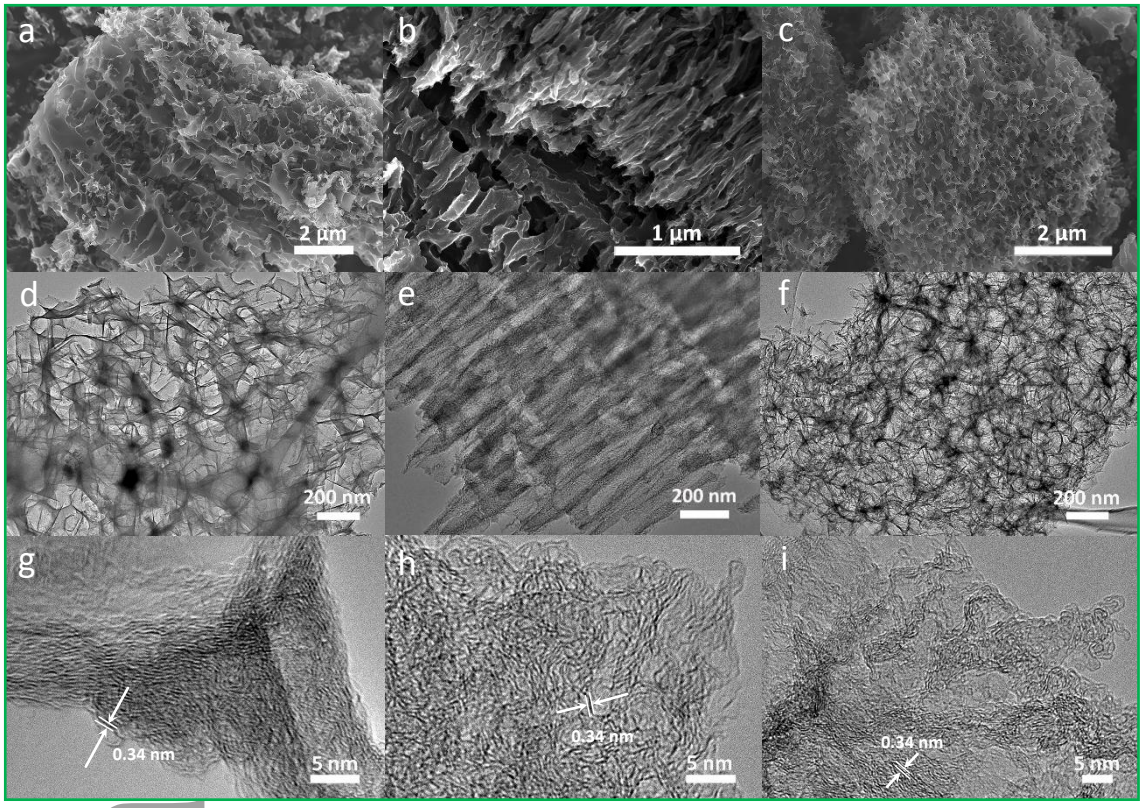

Figure 1. EM images of the three porous carbons. (a-c) SEM images, (d-f) TEM images, (g-i) HRTEM images. Wherein, a, d, g) PC; b, e, h) NC-2; c, f, i) NSC.

Scanning electron microscopy (SEM) images (**Figure 1**a and S1a**)** of PC confirm that it is highly porous. Transmission electron microscopy (TEM) further reveals that uniform, honeycomb-like pores in PC form a three-dimensionally interconnected network (Figure 1d and S1b). NCs (nitrogen-doped carbons derived from urea, sodium bicarbonate and glucose) with increasing N loadings are referred as NC-1, NC-2 and NC-3, respectively. Interestingly, NCs not only possess numerous pores, but also exhibit a pillaring layered structure, which are different from PC (Figure 1b, e and S2-4). Moreover, small rounded pores in NCs exist along the layered pore channels. However, the involvement of

thiourea did not change the pore frameworks and the pore shapes in NSC (Figure 1c, f and S5), compared to PC. As shown in the high-resolution transmission electron microscopy (HRTEM) images, multiple randomly oriented graphitic layers can be clearly seen in the pore frameworks of all porous carbon samples, with an identified interlayer spacing of 0.34 nm, which can be assigned to the (002) of graphite. This result suggests the high ratio of sp^2-C, which can also be verified by carbon EELS analysis (**Figure 2**a-d).

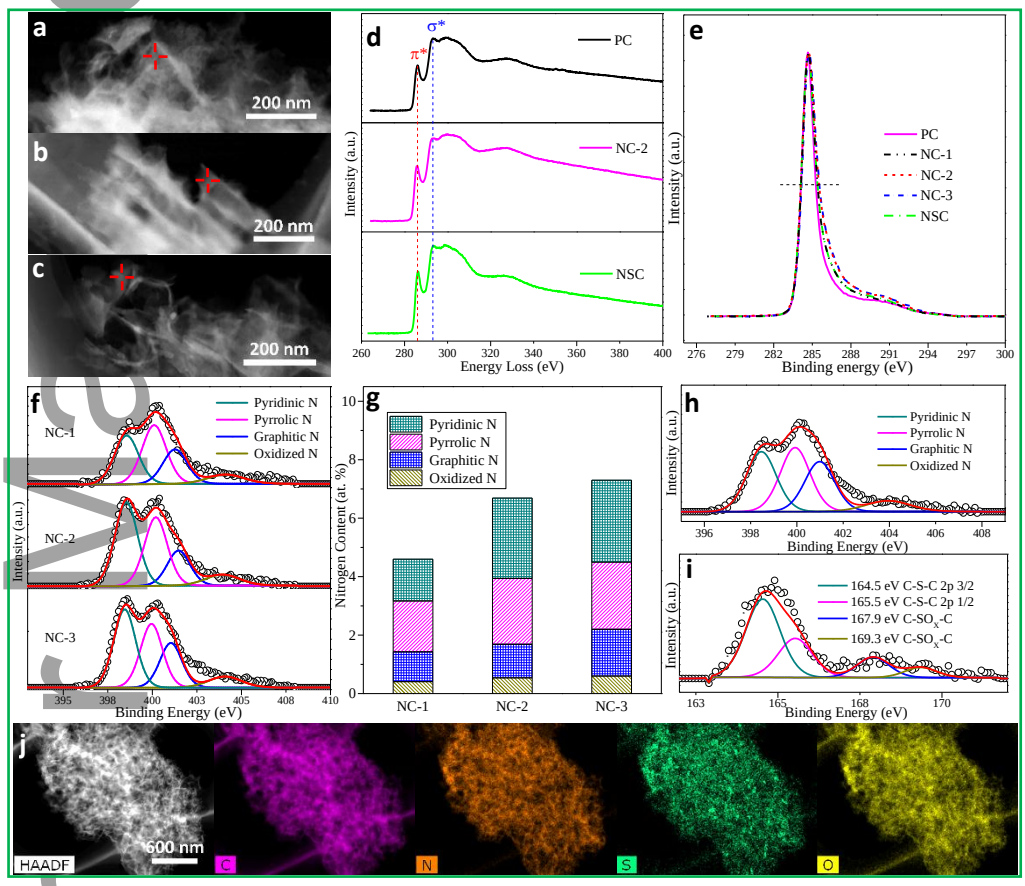

Figure 2. Dark field STEM images of a) PC, b) NC-2 and c) NSC; d) Electron energy-loss spectroscopy (EELS) spectra obtained at the marked points in a-c; e) High resolution N 1s spectra of all the porous carbons; f) High resolution N 1s spectra of NCs; g) The contents of four nitrogen species in NCs; h)

High resolution N 1s spectra of NSC; i) S 2p spectra of NSC; j) High angle annular dark field scanning TEM images (HAADF-STEM) and corresponding energy-dispersive X-ray spectroscopy (EDX) elemental mapping images of NSC.

The carbon K-edge spectra of the PC, NC-2 and NSC exhibit sharply-defined peaks at around 285.8 eV due to transitions from the 1s to the π* states, followed by the peaks at about 293.1 eV due mainly to transitions from 1s to σ* states, corresponding to the sp^2-hybridization states.[25-28] The strong and sharp π* peaks prove the high sp^2-C ratios in the porous carbons,[26, 29] consistent with the HRTEM observation. Since sp^2 bonding is correlated to the electrical conductivity,[23] the synthesized porous carbons are of high quality with an interconnected open-pore system, which can easily activate the electron transfer for electrochemical energy applications.

X-ray photoelectron spectroscopy (XPS) was employed to analyze the surface chemical states and the composition of the samples. According to previous studies, the introduction of heteroatoms into pristine carbon tends to produce more structural defects, reflected by the broadened FWHM (full width at half maximum) of C 1s peaks.[27, 28] Accordingly, NCs and NSC show slightly wider FWHMs than PC (Figure 2e). The tails between 286 and 292 eV can be ascribed to the surface carbon-oxygen, carbon-nitrogen or carbon-sulfur-containing groups and energy loss “shake-up” features.[27, 29, 30] However, the changes in the overall degree of graphitization of the porous carbons induced by heteroatom-doping were not appreciable, evidenced by the minor differences in I_D/I_G ratios obtained by the Raman spectra (Figure S6b). The N contents were found to be 4.5 at.% in NC-1, 6.7 at.% in NC-

2 and 7.3 at.% in NC-3 (Figure S6). NSC possesses a similar surface N content to NC-1 (4.6 at.%). In addition, the elemental mapping analysis of NC-2 and NSC shows that the chemical distributions of these elements along the pore frameworks are uniform (Figure 2j and S7). For NCs and NSC, the XPS N1s spectra can be fitted into four peaks with the binding energies at around 398, 400, 401 and 405 eV, corresponding to pyridinic-N, pyrrolic-N, graphitic-N, and oxidized-N, respectively.[31, 32] Except for the almost unchanged oxidized-N, the other N species show an increase trend in NCs with increasing total N content. It was documented that pyrrolic-N generally has a greater contribution to CO_2 capture than other species,[2, 33, 34] whereas graphitic-N and pyridinic-N are the most active sites in ORR.[32, 35] The high resolution S 2p peaks can be fitted into four peaks centred at around 164.5, 165.5, 167.9 and 169.3 eV, respectively. The former two peaks correspond to S $2p_{3/2}$ and S $2p_{1/2}$ positions of thiophene-S (-C-S-C-), while the peaks at 167.9 and 169.3 eV can be assigned to oxidized-S groups (-C-SO_x-C-).[30, 32, 36] The oxidized-S plays a significant role in CO_2 adsorption,[37] yet it is chemically inactive for ORR where thiophene-S is believed to be more effective.[38] The chemical compositions of the prepared samples suggested the functional groups potentially active for both CO_2 uptake and ORR.

According to our previous finding,[24] pure glucose decomposition has two peaks at 209 and 305 °C in DTG curve while glucose/sodium bicarbonate and glucose/bicarbonate/thiourea only have one peak at about 150 °C. Consistent with that, the DTG curve of the glucose/sodium bicarbonate/urea mixture (Figure S8) suggested the occurrence of the evaporation-induced self-assembly process among the precursors before pyrolysis, as it has only one decomposition peak at around 180 °C.

The dependence of the pore formation mechanism on hydrogen-bond interaction during the evaporation process of different precursor materials has been discussed. Based on reference [39], the hydrogen-bonding interactions of urea, water and bicarbonate ions are described in **Scheme 1**a. Specifically, urea, water molecules and hydrogen carbonate anions are linked alternately side by side via N-H···O and O-H···O hydrogen bonds to form a ribbon. Cross-linkage between adjacent ribbons generates a puckered urea-anion-water (HCO_3^-•$(NH_2)_2CO$•$2H_2O$) layer and two-dimensional network is built as a result. Scheme 1b describes several layers of such a network. On the other hand, preliminary findings showed that glucose solutions can be thermally decomposed under an excessive heat, causing the formation of 5-hydroxymethylfurfural (5-HMF) during evaporation at 105 ºC.[40] It is proposed that the formed 5-HMF might be alternately arranged and sandwiched between the adjacent HCO_3^-•$(NH_2)_2CO$•$2H_2O$ layers, bridged by O-H···O, H-O···H and O···H-N hydrogen bonds, as shown in Scheme 1c. Finally, during the pyrolysis of the mixture, 5-HMF is dehydrated and then carbonized to form the wall of pillaring-layered pores. Urea and sodium bicarbonate transformation, together with water molecules escaping, lead to the formation of the pillared-layered pore channels, which may also generate the cross-sectional pores in the channel walls (Scheme 1d). Since urea decomposition will leave small amount of carbon residues, some pores could also be observed on the channels of NCs.

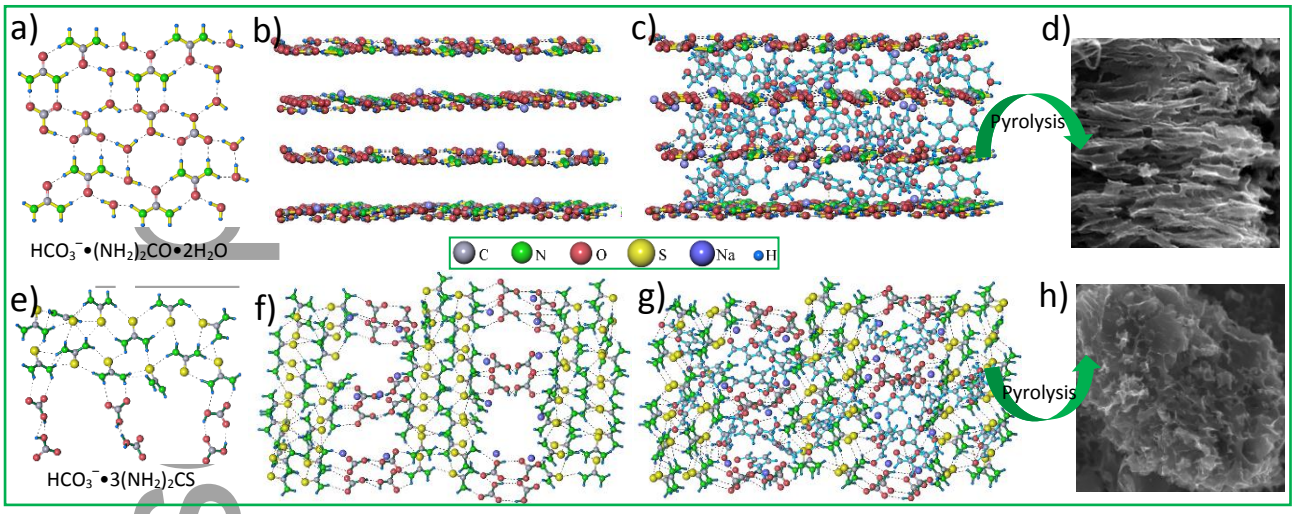

Scheme 1. Stereo drawing of the formation mechanism of (a-d) N-doped pillared-layered porous carbon and (e-h) N-S co-doped honeycomb-porous carbon.

Scheme 1e illustrates the hydrogen-bonding interactions among the thiourea molecules and bicarbonate ions.[41] Thiourea molecules are connected in turn by the pairs of N-H···S hydrogen bonds to form a zigzag ribbon. Unlike Scheme 1a, there is a highly twisted shape in this process. Twisted thiourea ribbons are jointed by lateral N-H···S to produce puckered double-ribbons, which are further cross-linked by $(HCO_3^-)_2$ units in a HCO_3^-•$3(NH_2)_2CS$ manner, resulting in a three-dimensional host-lattice with open channels (Scheme 1f). 5-HMF is closely involved in the host lattice by O-H···O, H-O···H, O-H···S and O···H-N hydrogen-bond-interactions, as shown in Scheme 1g. During the heating process, 5-HMF, thiourea and sodium bicarbonate decomposed, and large amount of pores are generated, resulting in a three-dimensional honeycomb pore network (Scheme 1h).

For the non-doped porous carbon without the involvement of urea or thiourea, it can be speculated that the pore structure in PC is formed following a similar principle, in which 5-HMF and HCO_3^- are cross-connected by O-H···O and H-O···H hydrogen bonds. The CO_2 formation and escaping lead to the highly-porous structures.

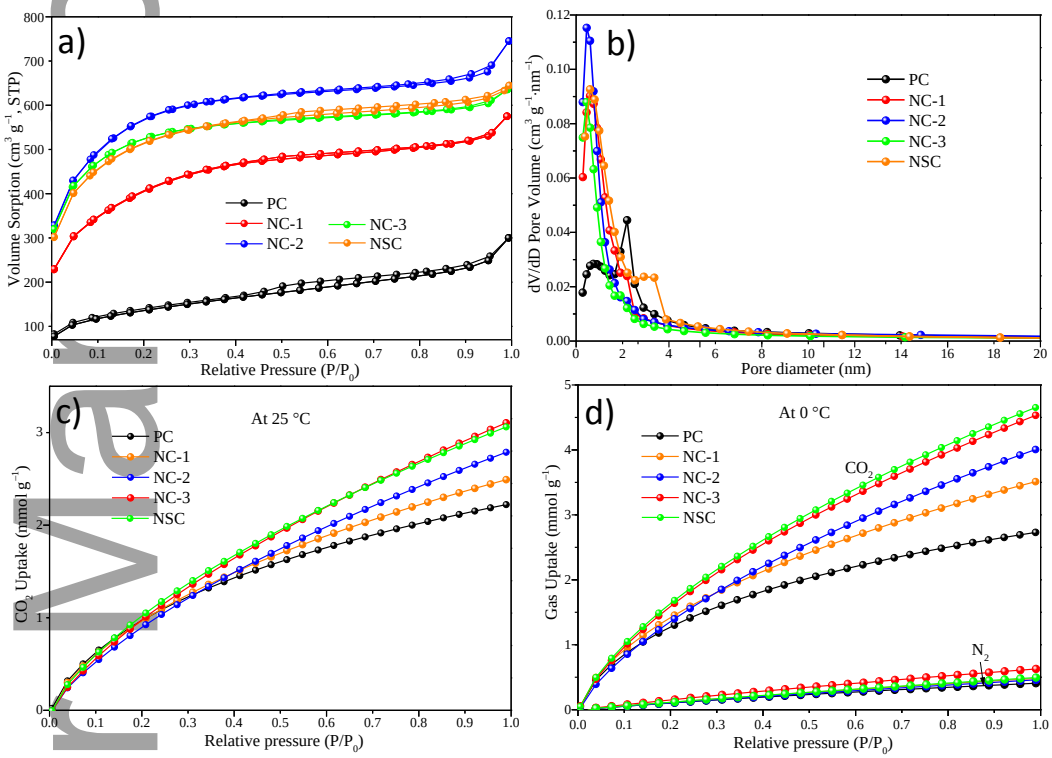

Figure 3. a) N_2 adsorption-desorption isotherms of the carbon samples, b) Pore size distributions calculated by BJH desorption, c) CO_2 adsorption isotherms on the as-prepared carbon samples at 25 °C and d) CO_2 and N_2 uptake isotherms at 0 °C under ambient pressure (1.0 atm).

To assess the textural properties of these carbons, N_2 adsorption-desorption isotherms were acquired and summarized in **Figure 3** and Table S1. The average pore sizes of all porous carbons are in a range of 0.28-50.6 nm, indicating hierarchical porosities with mesopores and micropores. Notably, after N or N, S doping, the BET surface areas of NCs (1344-1840 $m^2 g^{-1}$) and NSC (1608 $m^2 g^{-1}$) are much larger than PC, and are accompanied by enlarged pore volumes. The results proved that urea or thiourea may have triple functions in the pore formation processes: as an extra pore-generating agent, second carbon source and dopant precursor. The comparisons among NCs indicate that increasing N content leads to a higher micropore volume (V_{mic}). However, the mesopore volume (V_{meso}) increases first, then decreases with further increasing N content due to the potential blocking of pore channels by adventitious species. Considering that micropores are usually favored for CO_2 adsorption, raising the N doping content might be a good way to obtain high CO_2 uptake capacities. On the other hand, increasing V_{mic} may increase the contact resistance from isolated carbon particles and limit the conductivity, which should be considered when designing electrode materials for ORR. Therefore, a suitable mesopore and micropore ratio needs to be carefully controlled according to different applications.

CO_2 sorption measurements were performed at 25 and 0 °C under an atmospheric pressure range (0-1 atm) to evaluate the gas sorption properties of the prepared porous carbons. Figure 3c and d show CO_2 uptake isotherms for the porous carbons and the capacity values are summarized in Table S1. PC shows a moderate CO_2 uptake capacity. With increasing N doping level, the adsorption capacity increased gradually for NCs. According to recent studies on N-decorated carbons, apart from the BET surface area and microporosity, N doping level and hydrogen bonding are two other

factors closely governing the CO_2 capture performance.[42] Specifically, the presence of N atoms in the carbon, with the most active pyrrolic-N,[2, 33] will increase the basicity by offering electron donor groups and facilitate their interactions with acidic CO_2. In addition, the introduction of N into a carbon surface will improve the hydrogen-bonding interactions between the C-H groups and CO_2 molecules, leading to a greater CO_2 uptake.[3] It is thus deduced that higher micropore volume and pyrrolic N content are generally responsible for the highest capacity of NC-3 among the NCs (3.1 mmol g^{-1} at 25 °C and 4.5 mmol g^{-1} at 0 °C), better than NC-2 with the highest S_{BET}. NSC displays a similar CO_2 uptake to NC-3 at 25 °C, yet slightly higher adsorption at 0 °C (4.8 mmol g^{-1}). This performance is among the best porous carbons and superior to most MOFs (Table S2). It is also worth noting that the selectivity of CO_2/N_2 of NSC outperforms NC-3 at 0 °C with a lower N_2 adsorption while demonstrating a slightly higher CO_2 capture (Figure 3d). Previous studies indicated that the selective CO_2 uptakes are mainly ascribed to the functional groups.[43] Given that NSC possesses a comparable surface area, a lower micropore volume and lower N content than NC-3, the higher CO_2 capture capacity and better selectivity can be attributed to the trace amount of doping S atoms, mainly as oxidized-S.[37] According to the calculations based on natural bonding orbitals, O in thiophene (–0.94) possesses a more negative charge than N in pyrrole (–0.59) affected by the highly positive charge of S in thiophene.[37] Thus, the attraction energy between $O_{thiophene}$ and C_{CO2} (+1.07) is higher than that of $N_{pyrrole}$ with C_{CO2}. As a result, NSC exhibited a better selectivity and a comparative CO_2 capture capacity with NC-3.

To determine the interaction strengths between the carbon samples and the adsorbed CO_2, isosteric heats of adsorption (Q_{st}) on all the porous carbons were obtained from CO_2 adsorption isotherms at

0 and 25 °C based on the Clausius-Clapeyron equation (Figure S9). The Q_{st} values of all samples are in the range of 14.7-21.5 kJ mol^{-1}, which show an increasing trend after N doping compared to unmodified PC. Furthermore, NSC exhibits the highest Q_{st} value among all the porous carbons, indicating the origin of its better selectivity for CO_2 over N_2.[44]

2.2. Electrocatalytic Performance

To evaluate the catalytic ORR performance, cyclic voltammetry (CV) tests were conducted on the as-prepared carbons and commercial Pt/C (20 wt.% Pt, Vulcan) reference catalyst in N_2- and O_2-saturated 0.1 M KOH aqueous solutions (Figure S10). In N_2 environment, the CV curves showed nearly rectangular shapes, as a result of the typical capacitive effect.[45] When O_2 was introduced, well-defined ORR peaks centred at around 0.72 V were observed on NCs, which are positive than that of PC. After N, S co-doping, the peak potential of NSC shifted to a more positive 0.75 V, suggesting a better ORR activity.[14] Similar trends were observed with linear sweep voltammetry (LSV) tests on a rotating-disk electrode (RDE), recorded at different rotating speeds from 225 to 2500 rpm (**Figure 4**a and S11). Due to the combined effects of N functionalities and mesopore/micropore ratio, NCs exhibited similar onset-potentials (0.84 V) and half-wave potentials ($E_{1/2}$, 0.69-0.71 V), positive than PC (Table S3). Remarkably, compared with the mono-atom doped NCs, NSC displayed a higher ORR activity, as evidenced by the onset-potential of 0.87 V and $E_{1/2}$ of 0.74 V, comparable to 0.94 and 0.83 V on reference Pt/C. In addition, the ORR reaction current of NSC was similar to Pt/C.

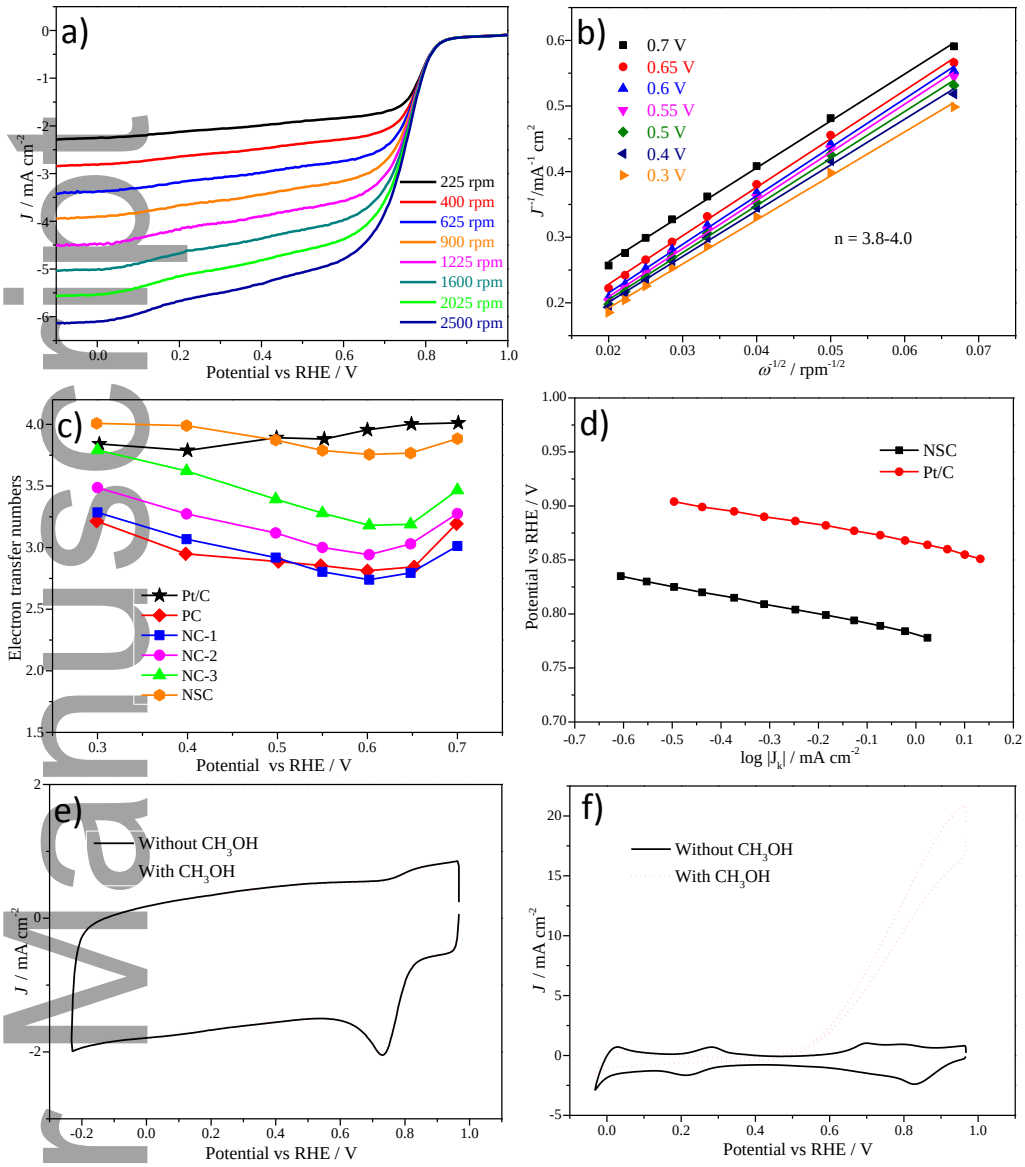

Figure 4. a) LSV curves (scan rate = 10 mV s^{-1}) for NSC in an O_2- saturated 0.1 M KOH electrolyte; b) K-L plots (J^{-1} versus $\omega^{-0.5}$) for NSC at different potentials; c) Electron-transfer numbers (n) of different samples calculated by their K-L plots; d) Tafel plots of NSC and Pt/C derived from their LSVs at 1600 rpm. CV curves of e) NSC and f) Pt/C in O_2- saturated 0.1 M KOH without and with 1.0 M CH_3OH (scan rate = 50 mV s^{-1}).

To qualify the ORR processes, Koutecky-Levich (K-L) plots (J^{-1} vs, $\omega^{-1/2}$) were obtained for each sample using the RDE at various rotating speeds. With increasing rotating speeds, the cathodic current was enlarged due to the improved mass transport at the electrode surface. Figure 4b shows K-L plots of NSC. The electron transfer numbers (n) were calculated by the slopes of the linear fitted K-L plots on the basis of the K-L equation. The n values of NSC were 3.8-4.0 at the potentials of 0.3-0.7 V, suggesting an electrochemically stable ORR process favored by a four-electron reduction pathway which directly reduces O_2 into OH^-. This is promising for the construction of fuel cells with a high efficiency. The electron transfer numbers of other samples were also calculated by the correspondingly fitted K-L plots (Figure S11), which are summarized in Figure 4c. With increasing N-doping levels in NCs, n increased, yet was still lower than NSC. Figure 4d shows the Tafel plots of NSC and commercial Pt/C, derived from Figure 4a and S11i. NSC has a Tafel slope of 87.0 mV/decade in 0.1 M KOH, close to the 81.1 mV/decade of Pt/C, indicating that NSC has an excellent kinetic process for ORR.[46] The tolerance of NSC and Pt/C toward methanol (MeOH) was determined by introducing 1.0 M MeOH into O_2 saturated 0.1 M KOH electrolyte.[46] Figure 4e shows almost no variation in the ORR peak current for NSC after adding MeOH, whereas significant oxidation current was observed in the CV of Pt/C catalyst (Figure 4f). This result suggests that NSC has a much better catalytic selectivity for ORR than Pt/C along with a strong tolerance to the crossover effect.[46]

Similar to most referenced carbon materials (Table S4), the onset potential and activity of NSC are still not as good as the commercial Pt/C, yet its high electrocatalytic efficiency and better selectivity

over methanol make it a promising candidate for the next generation of cost-effective ORR electrocatalysts.

2.3. Supercapacitor and Transport Characterization

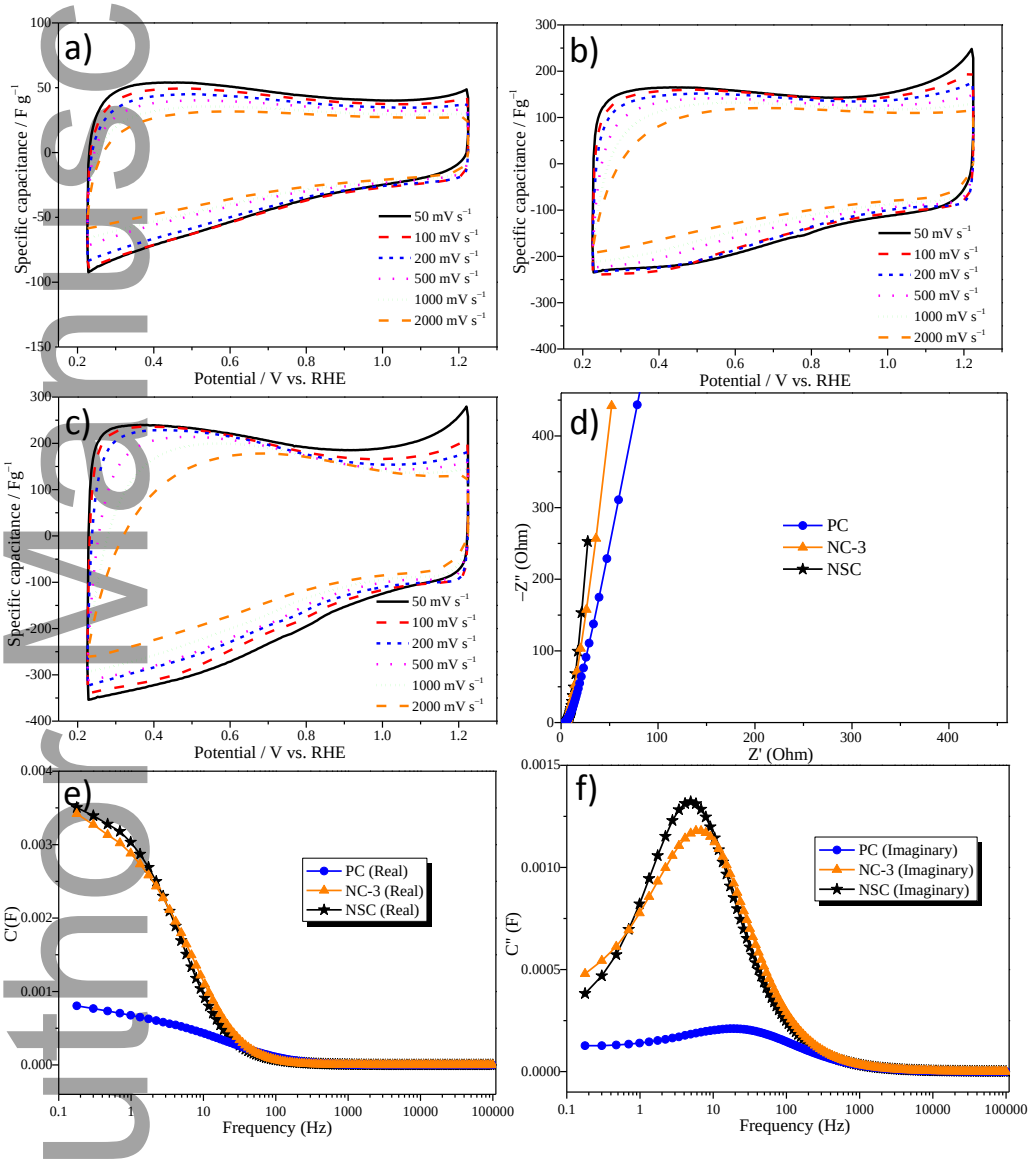

Figure 5. CV curves in 1 M KOH with different scan rates of a) PC, b) NC-3 and c) NSC; d) Nyquist plots of EIS measurements; e) Real and f) Imaginary capacitance plots for the complex capacitance analysis.

To investigate the transport issues in ORR activity, supercapacitor measurements were conducted. According to CVs measured in 1 M KOH at different scan rates, PC, NC-3 and NSC showed similar quasi-rectangular shapes (**Figure 5**a-c). It is noteworthy that the specific capacitances of these samples showed minor deactivation even up to an extremely high rate of 2000 mV s^{-1}, which was comparable to or better than previous results with superior rate performance.[26, 47] The rate performance is closely related to transport issues, which indicate the porous carbons synthesized in this work have excellent mass transport properties. Electrochemical impedance spectroscopy (EIS) (Figure 5d) further confirmed this point, because the three samples featured small arcs in the high frequency region, reflecting the low charge transfer resistance and well-defined electrical conductivity contributed by the interconnected pore framework and high sp^2-C ratio.[14, 26] As the three samples possess outstanding mass transport properties, the better ORR activities of NC-3 and NSC than pristine PC highlight the importance of heteroatom functionality.

As an alternative approach to analyze the supercapacitor frequency behavior, the real and imaginary parts of the capacitance were analyzed using the impedance data based on the following equations:[48]

$$Z(\omega)=\frac{1}{j\omega C(\omega)} \quad (1)$$

$$Z(\omega)=Z'(\omega)+jZ''(\omega) \quad (2)$$

$$C(\omega)=C'(\omega)-jC''(\omega) \quad (3)$$

$$C'(\omega)=-\frac{Z''(\omega)}{\omega|Z(\omega)|^2} \quad (4)$$

$$C''(\omega)=\frac{Z'(\omega)}{\omega|Z(\omega)|^2} \quad (5)$$

where Z′(ω) and Z″(ω) are the real and imaginary parts of the impedance, respectively; C′(ω) and C″(ω) represent the real and imaginary parts of the accessible capacitance, respectively. As shown in Figure 5e, C′(ω) sharply increases when the frequency decreases, then it is less dependent on frequencies. This is the feature of conversion from the electrode structure to electrode/electrolyte interface.[48] C″(ω) is related to the energy loss due to the irreversible process of the electrode, such as IR drop and Faradaic charge transfer. As shown in Figure 5f, C″(ω) goes through a maximum at peak frequency (f_0), defining a relaxation time constant ($\tau_0 = (2\pi f_0)^{-1}$), which reflects the kinetic performance of the supercapacitor.[49] Interestingly, PC, NC-3, and NSC show peaks at 22.0, 6.4 and 5.0 Hz, indicating the relaxation time of ~0.045, 0.16 and 0.20 s, respectively. In other words, PC is able to discharge its stored energy with high efficiency, 3.6 and 4.4 times faster than NC-3 and NSC. The electron and ion transport can be correlated to O_2 transport issues in ORR. Considering that NSC and NC-3 possess similar surface area, adjacent electrical conductivity properties deduced from their close relaxation time, whereas NSC has a lower N content, better ORR performance of NSC

emphasizes the excellent synergistic effect of N, S co-doping than solely N-doping for ORR catalysis. Therefore, compared to transport issues and BET surface areas, it is spectulated that surface functionality plays a more important role in our synthesized porous carbons, which needs to be enhanced to achieve the best ORR performance. In future research endeavours, more efforts will be made to further improve the overall properties, such as adopting KOH or NH_3 activation,[14, 15] or decoration with non-precious metallic compounds.[50]

3. Conclusions

In summary, we demonstrate a facile and scalable strategy to prepare heteroatom-doped, pillared-layered and/or honeycomb-like, porous carbons with high graphitic degrees, interconnected networks and high surface areas. The pore framework shapes, heteroatom functionalities, mesopore/micropore ratio and surface areas can be feasibly and rationally tailored. The as-prepared porous carbons show excellent CO_2 uptake capacities, high-rate performance and outstanding ORR activities as Pt-free catalysts in alkaline media. It is believed that this work is important for the design and large-scale production of porous carbons via a benign route, which implies promising applications in gas separation and energy storage/conversion.

4. Experimental Section

Chemical Reagents: D-(+)-glucose (≥ 99.5%), urea (≥ 99.5%), sodium bicarbonate (≥ 99.7%), thiourea (≥ 99.0%), Nafion® 117 solution (5wt.%, Aldrich), potassium hydroxide (≥ 70%, 30% water),

isopropanol alcohol (≥ 99.7%), methanol (≥ 99.9%), commercial Pt/C (20 wt.%, Vulcan) were purchased from Sigma-Aldrich and used directly without further purification.

Preparation of Porous Carbon Materials: (1) dissolve glucose (0.9 g), sodium bicarbonate (0.9 g) and urea (the mass changed from 0.3, 0.9 to 1.2 g to synthesize NC-1, NC-2 and NC-3, respectively) in pure water and then evaporate the water at 105 ^{o}C; (2) heat treatment of the mixture at 700 ^{o}C for 2 h with a heating rate of 5 ^{o}C min^{-1} under N_2 flow to form NCs. PC and NSC were prepared according to our previous reported method.[24] Briefly, pyrolysis of the mixture (PC) of glucose (0.9 g) and sodium bicarbonate (0.9 g) as well as these two chemicals with thiourea (0.3 g NSC) at 700 ^{o}C. Finally, the carbonized materials were grinded and washed with water and ethanol for several times, then dried in an oven.

Characterizations: N_2 adsorption-desorption isotherm was obtained on Micromeritics Tristar 3000 at −196 °C. SEM images were recorded on a FEI Verios XHR 460. TEM and HRTEM images were measured on JEOL 2100. The carbon EELS spectrum, HAADF-STEM and EDX elemental mapping were characterized by FEI Titan G2 80-200 TEM/STEM. XPS analysis was carried out on a Kratos Axis Ultra DLD system under ultra-high vacuum (UHV) conditions.

CO_2 Adsorption at 0 and 25 °C: The adsorption isotherms of each sample over pure CO_2 (99.999%) were recorded by a Micromeritics instrument (Gemini I-2360) at 0 and 25 ºC under low pressure up to 760 mmHg. All samples were degassed at 110 °C overnight before the tests. N_2 adsorption isotherm at 0 °C was also measured on this instrument to view the relative CO_2 selective adsorption.

Electrode Preparation for Electrochemical Measurements: The as-prepared porous carbons (2 mg) were grinded firstly and then blended with isopropanol (500 µL) and Nafion® 117 solution (25 µL) to

form a suspension (3.6 mg mL^{-1}) by sonication. Then, the catalyst ink (9 µL, containing 32.4 µg of catalyst) was dipped onto the surface of a pre-polished glassy carbon electrode (5.0 mm in diameter) and dried in air. For comparison, commercial Pt/C (20 wt.%, Vulcan) was also prepared by a similar procedure with the same loading on the surface of working electrode.

Electrochemical measurements were conducted using a MSR-RDE rotating disk (Pine Instrument Company, USA) controlled with a Zennium electrochemical workstation (Zahner, Germany) under ambient conditions. A three-electrode system was used with Ag/AgCl (KCl sat.) electrode and platinum wire as the counter electrode and the reference electrode, respectively, and a rotating disk electrode (RDE) with a glassy carbon as the working electrode. The potential differences between Ag/AgCl and reversible hydrogen electrode (RHE) were calibrated through equation (6):

$$E_{RHE} = E_{Ag/AgCl} + 0.059\,pH + 0.197 \qquad (6)$$

All potential data in this study refer to that of RHE.

ORR Measurements: CV experiments of different catalysts were performed in N_2/O_2-saturated KOH (0.1 M) solution at a scan rate of 50 mV s^{-1}. All electrochemical data were recorded until stable curves were obtained. For the RDE tests, the working electrode was conducted at a sweep rate of 10 mVs^{-1} with varying rotating speeds from 225 to 2500 rpm. All sample tests were repeated at least 3 times to avoid any incidental errors.

The Koutecky-Levich (K-L) plots (J^{-1} vs $\omega^{-1/2}$) were obtained according to linear fitting of the reciprocal rotating speed versus reciprocal current density at various electrode potentials. The overall electron transfer numbers (n) per oxygen molecule during a typical ORR process were calculated according to the slopes of linear fit lines in the K-L plots, on the basis of the Koutecky-Levich equations:[11]

$$1/J = 1/J_K + 1/B\omega^{1/2} \qquad (7)$$

$$B = 0.2nFC_0D_0^{2/3}\nu^{-1/6} \qquad (8)$$

where J is the measured current density, J_K the kinetic current density, ω the electrode rotating speed in rpm, B the reciprocal slopes of the K-L plots, n transferred electron number per oxygen molecule and the constant 0.2 is used when the rotating speed is in rpm. For the Tafel plots, J_K was determined from the mass-transport correction of RDE at 1600 rpm by equation (9):

$$J_K = (J * J_L)/(J_L - J) \qquad (9)$$

where J_L is the diffusion-limiting current density.

Supercapacitor and EIS: Supercapacitor performance was evaluated by measuring CVs in 1 M KOH with N_2 purging using the same electrical devices and procedures as described above. EIS was measured from 10 mHz to 100 KHz.

Supporting Information

Supporting Information is available from the Wiley Online Library or from the author.

Acknowledgments

W. Tian and H. Zhang contribute equaly to this paper. This work was supported by the Australian Research Council (DP130101319 and DP150103026). The authors acknowledge the assistance from The University of Western Australia Centre for Microscopy, Characterisation and Analysis, and also help from the WA X-Ray Surface Analysis Facility of Curtin University. H.S. thanks the Opening Project (KL-13 02) funded by State Key Laboratory of Materials-Oriented Chemical Engineering, Nanjing Tech University.

References

[1] N. L. Bindoff, P. A. Stott, K. M. AchutaRao, M. R. Allen, N. Gillett, D. Gutzler, K. Hansingo, G. Hegerl, Y. Hu, S. Jain, I. I. Mokhov, J. Overland, J. Perlwitz, R. Sebbari, X. Zhang, in *Climate Change 2013: The Physical Science Basis. Contribution of Working Group I to the Fifth Assessment Report of the Intergovernmental Panel on Climate Change*, (Eds: T. F. Stocker, D. Qin, G.-K. Plattner, M. Tignor, S. K. Allen, J. Boschung, A. Nauels, Y. Xia, V. Bex, P. M. Midgley), Cambridge University Press, Cambridge, United Kingdom and New York, NY, USA **2013**, 867.

[2] M. Sevilla, P. Valle-Vigon, A. B. Fuertes, *Adv. Funct. Mater*. **2011**, *21*, 2781.

[3] W. Xing, C. Liu, Z. Y. Zhou, L. Zhang, J. Zhou, S. P. Zhuo, Z. F. Yan, H. Gao, G. Q. Wang, S. Z. Qiao, *Energy Environ. Sci.* **2012**, *5*, 7323.

[4] G. T. Rochelle, *Science* **2009**, *325*, 1652.

[5] P. Markewitz, W. Kuckshinrichs, W. Leitner, J. Linssen, P. Zapp, R. Bongartz, A. Schreiber, T. E. Muller, *Energy Environ. Sci.* **2012**, *5*, 7281.

[6] R. Vaidhyanathan, S. S. Iremonger, G. K. H. Shimizu, P. G. Boyd, S. Alavi, T. K. Woo, *Science* **2010**, *330*, 650.

[7] W. Morris, B. Leung, H. Furukawa, O. K. Yaghi, N. He, H. Hayashi, Y. Houndonougbo, M. Asta, B. B. Laird, O. M. Yaghi, *J. Am. Chem. Soc.* **2010**, *132*, 11006.

[8] M. Sevilla, A. B. Fuertes, *Energy Environ. Sci.* **2011**, *4*, 1765.

[9] H. Furukawa, O. M. Yaghi, *J. Am. Chem. Soc.* **2009**, *131*, 8875.

[10] W. Xia, A. Mahmood, Z. B. Liang, R. Q. Zou, S. J. Guo, *Angew. Chem. Int. Ed..* **2016**, *55*, 2650.

[11] Y. Y. Liang, Y. G. Li, H. L. Wang, J. G. Zhou, J. Wang, T. Regier, H. J. Dai, *Nat. Mater.* **2011**, *10*, 780.

[12] G. Wu, K. L. More, C. M. Johnston, P. Zelenay, *Science* **2011**, *332*, 443.

[13] M. K. Debe, *Nature* **2012**, *486*, 43.

[14] W. H. He, C. H. Jiang, J. B. Wang, L. H. Lu, *Angew. Chem. Int. Ed..* **2014**, *53*, 9503.

[15] H. W. Liang, X. Zhuang, S. Brüller, X. Feng, K. Müllen, *Nat. Commun.* **2014**, *5*.

[16] M. Kwiatkowski, A. Policicchio, M. Seredych, T. J. Bandosz, *Carbon* **2016**, *98*, 250.

[17] J. Liang, Y. Jiao, M. Jaroniec, S. Z. Qiao, *Angew Chem. Int. Ed..* **2012**, *51*, 11496.

[18] J. W. F. To, J. J. He, J. G. Mei, R. Haghpanah, Z. Chen, T. Kurosawa, S. C. Chen, W. G. Bae, L. J. Pan, J. B. H. Tok, J. Wilcox, Z. N. Bao, *J. Am. Chem. Soc.* **2016**, *138*, 1001.

[19] E. Proietti, F. Jaouen, M. Lefevre, N. Larouche, J. Tian, J. Herranz, J. P. Dodelet, *Nat. Commun.* **2011**, *2*.

[20] Q. Shi, R. Y. Zhang, Y. Y. Lu, Y. H. Deng, A. A. Elzatahrya, D. Y. Zhao, *Carbon* **2015**, *84*, 335.

[21] W. Luo, Y. Wang, S. Chou, Y. Xu, W. Li, B. Kong, S. X. Dou, H. K. Liu, J. Yang, *Nano Energy* **2016**, *27*, 255.

[22] a) W. Li, J. Liu, D. Zhao, *Nat. Rev. Mater.* **2016**, 16023; b) W. Luo, Y. H. Li, J. P. Dong, J. Wei, J. Q. Xu, Y. H. Deng, D. Y. Zhao, *Angew. Chem. Int. Ed..* **2013**, *52*, 10505.

[23] J. Wei, D. D. Zhou, Z. K. Sun, Y. H. Deng, Y. Y. Xia, D. Y. Zhao, *Adv. Funct. Mater*. **2013**, *23*, 2322.

[24] W. J. Tian, H. Y. Zhang, X. G. Duan, H. Q. Sun, M. O. Tade, H. M. Ang, S. B. Wang, *ACS Appl. Mater. Interfaces* **2016**, *8*, 7184.

[25] S. D. Berger, D. R. Mckenzie, P. J. Martin, *Philos. Mag. Lett.* **1988**, *57*, 285.

[26] D. Y. Chung, K. J. Lee, S. H. Yu, M. Kim, S. Y. Lee, O. H. Kim, H. J. Park, Y. E. Sung, *Adv. Energy Mater.* **2015**, *5*.

[27] Y. M. Lin, X. L. Pan, W. Qi, B. S. Zhang, D. S. Su, *J. Mater. Chem. A* **2014**, *2*, 12475.

[28] Y. J. Cho, H. S. Kim, S. Y. Baik, Y. Myung, C. S. Jung, C. H. Kim, J. Park, H. S. Kang, *J. Phys. Chem. C* **2011**, *115*, 3737.

[29] Y. W. Zhu, S. Murali, M. D. Stoller, K. J. Ganesh, W. W. Cai, P. J. Ferreira, A. Pirkle, R. M. Wallace, K. A. Cychosz, M. Thommes, D. Su, E. A. Stach, R. S. Ruoff, *Science* **2011**, *332*, 1537.

[30] W. T. Gu, M. Sevilla, A. Magasinski, A. B. Fuertes, G. Yushin, *Energy Environ. Sci.* **2013**, *6*, 2465.

[31] a) L. T. Qu, Y. Liu, J. B. Baek, L. M. Dai, *ACS Nano* **2010**, *4*, 1321; b) Y. Wang, Y. Y. Shao, D. W. Matson, J. H. Li, Y. H. Lin, *ACS Nano* **2010**, *4*, 1790.

[32] C. Han, X. J. Bo, Y. F. Zhang, M. A. Li, L. P. Guo, *J. Power Sources* **2014**, *272*, 267.

[33] J. R. Pels, F. Kapteijn, J. A. Moulijn, Q. Zhu, K. M. Thomas, *Carbon* **1995**, *33*, 1641.

[34] R. Z. Bai, M. L. Yang, G. S. Hu, L. Q. Xu, X. Hu, Z. M. Li, S. L. Wang, W. Dai, M. H. Fan, *Carbon* **2015**, *81*, 465.

[35] a) L. F. Lai, J. R. Potts, D. Zhan, L. Wang, C. K. Poh, C. H. Tang, H. Gong, Z. X. Shen, L. Y. Jianyi, R. S. Ruoff, *Energy Environ. Sci.* **2012**, *5*, 7936; b) D. Guo, R. Shibuya, C. Akiba, S. Saji, T. Kondo, J. Nakamura, *Science* **2016**, *351*, 361.

[36] J. F. Moulder, J. Chastain, *Handbook of X-ray Photoelectron Spectroscopy: A Reference Book of Standard Spectra for Identification and Interpretation of XPS Data*, Physical Electronics Division, Perkin-Elmer Corporation, **1992**.

[37] H. Seema, K. C. Kemp, N. H. Le, S. W. Park, V. Chandra, J. W. Lee, K. S. Kim, *Carbon* **2014**, *66*, 320.

[38] S. B. Yang, L. J. Zhi, K. Tang, X. L. Feng, J. Maier, K. Mullen, *Adv. Funct. Mater*. **2012**, *22*, 3634.

[39] C. K. Lam, T. C. Mak, *J. Struct. Chem.* **1999**, *40*, 714.

[40] N. E. Webb, G. J. Sperandio, A. N. Martin, *J. Pharm. Sci.* **1958**, *47*, 101.

[41] Q. Li, T. C. W. Mak, *J. Inclusion Phenom. Mol. Recognit. Chem.* **1994**, *20*, 73.

[42] G. Sethia, A. Sayari, *Carbon* **2015**, *93*, 68.

[43] Q. G. Zhai, N. Bai, S. N. Li, X. H. Bu, P. Y. Feng, *Inorg. Chem.* **2015**, *54*, 9862.

[44] A. Aijaz, N. Fujiwara, Q. Xu, *J. Am. Chem. Soc.* **2014**, *136*, 6790.

[45] W. Yang, T. P. Fellinger, M. Antonietti, *J. Am. Chem. Soc.* **2011**, *133*, 206.

[46] W. X. Yang, X. J. Liu, X. Y. Yue, J. B. Jia, S. J. Guo, *J. Amer. Chem. Soc.* **2015**, *137*, 1436.

[47] a) L. Qie, W. M. Chen, H. H. Xu, X. Q. Xiong, Y. Jiang, F. Zou, X. L. Hu, Y. Xin, Z. L. Zhang, Y. H. Huang, *Energy Environ. Sci.* **2013**, *6*, 2497; b) Y. L. Cheng, L. Huang, X. Xiao, B. Yao, L. Y. Yuan, T. Q. Li, Z. M. Hu, B. Wang, J. Wan, J. Zhou, *Nano Energy* **2015**, *15*, 66.

[48] P. L. Taberna, P. Simon, J. F. Fauvarque, *J. Electrochem. Soc.* **2003**, *150*, A292.

[49] J. Lim, U. N. Maiti, N. Y. Kim, R. Narayan, W. J. Lee, D. S. Choi, Y. Oh, J. M. Lee, G. Y. Lee, S. H. Kang, H. Kim, Y. H. Kim, S. O. Kim, *Nat. Commun.* **2016**, *7*.

[50] a) J. Masa, W. Xia, M. Muhler, W. Schuhmann, *Angew. Chem. Int. Ed.*. **2015**, *54*, 10102; b) J. X. Zhao, Z. F. Chen, *J. Phys. Chem. C* **2015**, *119*, 26348.

List of Figure Captions

Figure 1. EM images of the three porous carbons. (a-c) SEM images, (d-f) TEM images, (g-i) HRTEM images. Wherein, a, d, g) PC; b, e, h) NC-2; c, f, i) NSC.

Figure 2. Dark field STEM images of a) PC, b) NC-2 and c) NSC; d) Electron energy-loss spectroscopy (EELS) spectra obtained at the marked points in a-c; e) High resolution N 1s spectra of all the porous carbons; f) High resolution N 1s spectra of NCs; g) The contents of four nitrogen species in NCs; h) High resolution N 1s spectra of NSC; i) S 2p spectra of NSC; j) High angle annular dark field scanning TEM images (HAADF-STEM) and corresponding energy-dispersive X-ray spectroscopy (EDX) elemental mapping images of NSC.

Figure 3. a) N_2 adsorption-desorption isotherms of the carbon samples, b) Pore size distributions calculated by BJH desorption, c) CO_2 adsorption isotherms on the as-prepared carbon samples at 25 °C and d) CO_2 and N_2 uptake isotherms at 0 °C under ambient pressure (1.0 atm).

Figure 4. a) LSV curves (scan rate = 10 mV s^{-1}) for NSC in an O_2- saturated 0.1 M KOH electrolyte; b) K-L plots (J^{-1} versus $\omega^{-0.5}$) for NSC at different potentials; c) Electron-transfer numbers (n) of different samples calculated by their K-L plots; d) Tafel plots of NSC and Pt/C derived from their LSVs at 1600 rpm. CV curves of e) NSC and f) Pt/C in O_2- saturated 0.1 M KOH without and with 1.0 M CH_3OH (scan rate = 50 mV s^{-1}).

Figure 5. CV curves in 1 M KOH with different scan rates of a) PC, b) NC-3 and c) NSC; d) Nyquist plots of EIS measurements; e) Real and f) Imaginary capacitance plots for the complex capacitance analysis.

Scheme 1. Stereo drawing of the formation mechanism of (a-d) N-doped pillared-layered porous carbon and (e-h) N-S co-doped honeycomb-porous carbon.

Table of Contents

N-doped layered and N, S co-doped honeycomb carbons have been fabricated, and the hydrogen-bond interactions during the self-assembly process are suggested to be responsible for the formation of different pore frameworks. The tailored micropore/mesopore architecture and heteroatoms doping of the porous carbons synegistically induce enhanced CO_2 capture capacity/selectivity and improved ORR activities.

Keywords: *Heteroatom-doping, Pillared-layer carbon, Honeycomb carbon, CO_2 capture, ORR*

Wenjie Tian, Huayang Zhang, Hongqi Sun, Alexandra Suvorova, Martin Saunders, Moses Tade, and Shaobin Wang**

Title: Heteroatom (N or N-S)-Doping Induced Layered and Honeycomb Microstructures of Porous Carbons for CO_2 Capture and Energy Applications

TOC Figure